Dipolar excitonic insulator in a moiré lattice

Jie Gu[1], Liguo Ma[1], Song Liu[2], Kenji Watanabe[3], Takashi Taniguchi[3], James C. Hone[2], Jie Shan[1,4,5*], Kin Fai Mak[1,4,5*]

[1]School of Applied and Engineering Physics, Cornell University, Ithaca, NY, USA
[2]Department of Mechanical Engineering, Columbia University, New York, NY, USA
[3]National Institute for Materials Science, Tsukuba, Japan
[4]Laboratory of Atomic and Solid State Physics, Cornell University, Ithaca, NY, USA
[5]Kavli Institute at Cornell for Nanoscale Science, Ithaca, NY, USA

*Email: jie.shan@cornell.edu; kinfai.mak@cornell.edu

Two-dimensional moiré materials provide a highly controllable solid-state platform for studies of quantum phenomena [1-4]. To date, experimental studies have focused on the correlated electronic states [5-13], whereas correlated bosonic states in moiré materials have received less attention. Here, we report a correlated dipolar excitonic insulator – a charge insulating state driven by exciton formation [14, 15]– in a device where a WSe_2 monolayer and a WSe_2/WS_2 moiré bilayer are coupled via Coulomb interactions. The system is a Mott insulator when all the holes reside in the moiré bilayer. Under an out-of-plane electric field, the holes can be continuously transferred to the WSe_2 monolayer, but remain strongly bound to the empty moiré sites, and effectively form an interlayer exciton fluid in the moiré lattice. We further observe the emergence of local magnetic moments in the WSe_2 monolayer induced by the strong interlayer Coulomb correlation. Our result provides a platform for realizing correlated quantum phenomena described by bosonic lattice models in a solid-state system, complementary to cold atom setups [16-21].

We consider a heterostructure of a WSe_2 monolayer and a WSe_2/WS_2 moiré (bi)layer that are separated by a thin hexagonal boron nitride (hBN) spacer (Fig. 1a). The spacer suppresses single-particle tunneling [22, 23] between the monolayer and the moiré layer, but is sufficiently thin (2-4 layers, thickness $d \approx 1$ nm) relative to the moiré period ($a_m \approx 8$ nm) so that the interlayer Coulomb interaction is as important as the Coulomb interaction within the moiré layer. We discuss the case of hole doping; the concept also applies to the case of electron doping. The valence band edge of the WSe_2/WS_2 bilayer resides in the constituent WSe_2 layer [10, 11]; it is above the band edge of the WSe_2 monolayer because of the moiré potential [12] (Fig. 1b). The flat moiré bands in angle-aligned WSe_2/WS_2 bilayers have been shown to realize the triangular lattice Fermi-Hubbard model in the strong correlation regime [9-12, 24, 25]. When the moiré layer is populated with one hole per moiré site and the monolayer is undoped, the system is an electronic Mott insulator (Fig. 1d, left). An out-of-plane electric field, E, which shifts the relative band alignment, can be tuned so that some holes are transferred from the moiré layer to the monolayer with the total hole density fixed (Fig. 1d, middle). The holes in the monolayer are bound to the empty moiré sites to minimize the Coulomb repulsion energy. Under a particle-hole transformation in the moiré layer, the empty sites become 'electrons'; excitons, bound states of holes in the monolayer valence band and electrons in the moiré Hubbard band, emerge. These interlayer excitons, which are strongly interacting, can hop around and form a fluid in the moiré lattice (Fig. 1d, right), in contrast to the Mott insulator in an isolated moiré layer, in which charges are frozen, and the reported exciton fluid in a continuum [22, 26]. It is also a zero-magnetic-field analogue of the exciton fluid in quantum Hall bilayers [27-29], induced by the moiré flat bands instead of the dispersionless Landau levels.

The interlayer excitons are tightly bound in the limit of low exciton density and $d \ll a_m$. Dissociation of an exciton corresponds to removing a hole from its pairing empty site and creating a doublon on another site. Ignoring extended Coulomb interactions, we estimate the exciton binding energy using the onsite Coulomb repulsion energy, $\frac{e^2}{4\pi\epsilon\epsilon_0 a_m} \sim 50$ meV (here e, $\epsilon \approx 4.5$ [12] and ϵ_0 denote the elementary charge, hBN effective dielectric constant and vacuum permittivity, respectively; and a_m approximates the hole Wannier function size). The ground state of the fluid is charge-incompressible [14, 15] but exciton-compressible in general [22]; perfect Coulomb drag is expected in the coupled monolayer and moiré layer [30]. The exciton density can be continuously varied by the electric field E. In the low exciton density or the BEC (Bose-Einstein condensation) regime, the exciton fluid is expected to transition from a normal fluid to a superfluid at sufficiently low temperatures and disorder densities [31-35]. The large exciton binding energy favors high transition temperature [34-38]. In the high exciton density or the BCS (Bardeen-Cooper-Schrieffer) regime, superfluidity and electron-hole binding are expected to occur at nearly the same transition temperature [39].

In this study, we demonstrate realization of equilibrium excitons in a lattice using the moiré heterostructure illustrated in Fig. 1a. Both 0- and 60-degree-aligned WSe_2/WS_2 bilayers (moiré density around 1.9×10^{12} cm^{-2}) have been studied; they show similar results. The heterostructure is dual-gated with nearly symmetric top and bottom gates made of hBN gate dielectrics and graphite gate electrodes. The two gate voltages (V_t and V_b for the top and bottom gates, respectively) tune independently the total hole density ν (measured in units of the moiré density) through $(V_t + V_b)$ and the out-of-plane electric field E through $(V_t - V_b)$. The holes are generally distributed in both the moiré layer (ν_m) and the monolayer (ν_f): $\nu = \nu_m + \nu_f$. We probe the correlation effects as a function of (ν, E) by optical spectroscopies and determine the charge gap energy by capacitance measurements. We further demonstrate charge localization and emergence of local magnetic moments in the monolayer induced by interlayer Coulomb correlation through magnetic circular dichroism (MCD) measurements. Details on the device fabrication and measurement methods are provided in Methods. Unless otherwise specified, all measurements are performed at 3.4 K.

Figure 1e, f illustrate the doping dependence of the optical reflection contrast and photoluminescence (PL) spectra of the heterostructure, respectively, at E = -34 mV/nm. We can identify in the reflection spectrum resonances from moiré excitons [40-46] and the 1s and 2s excitons of the monolayer (Fig. 1c is the spectrum at zero-doping). The PL around 1.4 eV arises from recombination of holes in WSe_2 and electrons in WS_2 of the moiré layer [11, 47] (linecuts at different ν's are shown in Extended Data Fig. 2). The PL intensity generally decreases with doping. At E = -34 mV/nm, holes are doped only into the moiré layer and the monolayer remains charge neutral for the entire doping range in Fig. 1e, f. This is supported by the ν-independent 1s exciton response of the monolayer. The 2s exciton of the monolayer has been demonstrated to be a sensitive probe of the charge insulating states in proximate materials [12]; it manifests a spectral blueshift with enhanced reflection contrast due to reduced dielectric screening of the excitonic interactions. We clearly identify five insulating states in the moiré layer, including the band insulator (ν = 0), Mott insulator (ν = 1), and electron crystals (ν = 1/3, 2/3, 1/2) in order of decreasing charge gap size. But the 2s exciton loses transition amplitude and sensitivity to correlated insulating states upon doping in the monolayer [12].

The correlated insulating states can also be identified by PL of the moiré layer with suppressed emission intensity and abrupt energy shift [11, 47]. The latter is presumably related to the chemical potential jump with doping across a correlated insulating state. Further theoretical studies are required to fully understand the microscopic mechanism. The spectral responses below $\nu \approx 1/3$ are likely distorted by the nonlinear gating effect from the non-ideal electrical contact to the heterostructure at low doping densities and low temperatures. Below we explore the (ν, E) parameter space for new correlated states using PL as a probe.

Figure 2a, b show the doping dependence of the reflection spectrum of the monolayer 1s exciton and the PL spectrum of the moiré layer, respectively, at four representative electric fields. At E = -10 mV/nm, the spectra for $\nu \leq 1$ resemble that of Fig. 1e, f. For ν > 1, the 1s exciton turns into an attractive polaron (redshifted branch, denoted as X^+) and a repulsive polaron (blueshifted branch, not labeled), which signal hole doping into the monolayer [23, 48]. The reflection change at ν = 1 is correlated with a local intensity minimum and an abrupt energy shift of the PL. As ν further increases, the PL follows a smooth doping dependence till $\nu \approx 1.8$ while X^+ remains nearly unchanged. These results indicate that the holes are first doped into the moiré layer to completely fill the first Hubbard band; further doping introduces holes into the monolayer till $\nu \approx 1.8$, at which the chemical potential reaches the second Hubbard band of the moiré layer. The state at ν = 1 is an electronic Mott insulator. For ν between 1 and 1.8, the doping density in the moiré layer is fixed at ν_m = 1.

At larger electric fields (E = 15 and 18 mV/nm), the polaron feature (X^+) appears at smaller ν's (< 1) in the reflection spectrum; accordingly, the extended region of ν_m = 1 emerges at larger ν's (> 1) in the PL spectrum. In addition, the electron crystal states can no longer be identified. These results support that the holes are now shared between the monolayer and the moiré layer before the density in the moiré layer reaches ν_m = 1. The electron crystal states are quantum melted [24] because the extended Coulomb repulsion in the moiré layer that induces these states is screened by the holes in the monolayer.

Remarkably, we observe an abrupt energy shift in both the attractive polaron resonance and the PL at total filling $\nu = 1$. This signifies a chemical potential jump [11, 49] and emergence of a new correlated insulating state. Such a state is unexpected if the monolayer and the moiré layer are uncoupled. In that case both layers should be charge-compressible. The state is consistent with a dipolar excitonic insulator induced by the strong interlayer Coulomb interaction (Fig. 1d): holes in the monolayer (ν_f) and in the moiré layer (ν_m) with $\nu_m + \nu_f = 1$ effectively form dipolar excitons with exciton density $\nu_X = \nu_f$. As electric field increases, the exciton density increases, the binding energy decreases, and the insulating state weakens. Above the exciton Mott density (around 1.4×10^{12} cm^{-2}, see measurement below), the exciton fluid turns into an electron-hole plasma [22, 36]. The state can no longer be observed at $E \gtrsim 30$ mV/nm.

The (ν, E) parameter space is mapped out for the excitonic insulating state in Fig. 3a, b. It can be divided into four electrostatic doping regions: (I) the monolayer is charge neutral (ν_f = 0); (II) the monolayer is doped and the moiré layer is at $\nu_m = 1$; (III) doping density in both layers is < 1 (region of interest); (IV) the moiré layer is charge neutral ($\nu_m = 0$). We use two spectral responses to identify these regions. The peak amplitude of the 1s exciton reflection is sensitive to doping in the monolayer [23, 48]. We determine the boundary between the neutral and doped monolayer (dash-dotted lines) in Fig. 3b. The PL exhibits an intensity minimum when the Fermi level touches a Hubbard band (both top and bottom) of the moiré layer. We determine the boundaries of the first Hubbard band (dashed lines) in Fig. 3a. Details on the doping region assignment and maps of other spectral responses, including the PL peak energy and the attractive polaron reflection intensity, are provided in Methods and Extended Data Fig. 6, 7.

The optical studies (Fig. 3a) suggest an excitonic insulator over a large range of electric field and a narrow range of doping density around total filling $\nu = 1$ in Region III. We characterize the state quantitatively by capacitance measurements. The capacitance device is similar to that of Fig. 1a with a local bottom gate (Extended Data Fig. 4a). The top gate dopes the contact region of the heterostructure heavily to achieve good electrical contacts while the local bottom gate tunes doping density in the sample of interest [50]. The accessible range of (ν, E) is thus limited in order to maintain good electrical contacts. The differential gate capacitance, C, is measured by collecting charges on the bottom gate while applying a small AC voltage on the heterostructure. We expect $C \approx C_g$ if the heterostructure is charge-compressible (conducting), and $C < C_g$ if it is charge-incompressible (insulating), with C_g denoting the geometrical bottom-gate-to-sample capacitance. Figure 3c is the measured C/C_g as a function of (ν, E) at 20 K and 443 Hz. The boundaries of different doping regions (dashed lines) are obtained from optical measurements on the same device. In Region III, we observe $C < C_g$ around total filling $\nu = 1$ over an extended range of electric field, and $C \approx C_g$ in the background. The charge-incompressible state revealed by capacitance is fully consistent with that from the optical studies of Fig. 3a and Extended Data Fig. 7. (The larger electric field values here compared to Fig. 3a, b are due to a thinner hBN spacer in the capacitance device.) The state persists up to around 120 K. Details on the capacitance measurements and results at other temperatures are included in Methods and Extended Data Fig. 4, 5.

We evaluate the charge gap of the excitonic insulator by integrating the capacitance dip [50], $\frac{e}{2}\int dV_b\left(1-\frac{C}{C_g}\right)$. Figure 3d summarizes the electric-field dependence of the charge gap at varying temperatures (in contrast, the charge gap of the electronic Mott insulator in bare WSe_2/WS_2 moiré bilayers is nearly independent of E [11]). The top axis shows the corresponding exciton density, ν_X, from electrostatics calculations. The smooth electric-field dependences show that the exciton fluid is compressible (that is, the holes can be continuously transferred between the layers). The gap energy at small exciton density and low temperature (around 30 meV) provides a measure of the exciton binding energy [22], which is consistent with our estimate based on the on-site repulsion energy. The charge gap vanishes at large ν_X's; at low temperature, it is around 0.7 (1.4×10^{12} cm^{-2}, also see Extended Data Fig. 7). This provides an estimate of the Mott density, beyond which the charge-incompressible excitonic insulator transitions into a charge-compressible electron-hole plasma at low temperatures [22, 36]. The large exciton binding energy, high Mott density and ionization temperature observed in our experiment are all consistent.

Finally, we demonstrate charge localization and emergence of local magnetic moments in the monolayer induced by the strong interlayer Coulomb correlation in the excitonic insulating state. We measure the magnetic response of the monolayer under an out-of-plane magnetic field by MCD near its repulsive polaron feature, which has been shown to be proportional to the sample magnetization [11, 51, 52]. Figure 4a shows the magnetic-field dependence of the MCD at $\nu_X\approx0.3$. The behavior at other exciton densities is similar. At 3.4 K, the MCD increases linearly with magnetic field under small fields, and saturates above 2 T. The saturation field increases rapidly with increasing temperature. The temperature dependence of the magnetic susceptibility, χ, extracted from the zero-field slope of the MCD [11, 51], follows the Curie-Weiss behavior $\chi^{-1}\propto T-\theta$ (line in Fig. 4b) with T and θ denoting the sample temperature and the Weiss constant, respectively. Such a behavior is in contrast to that of an isolated monolayer at comparable hole doping densities [11, 52, 53] but compatible with that of local magnetic moments [11, 51] induced by exciton formation. The Weiss constant obtained from the fits (solid lines) changes from ~ 0 to - 2 K when the exciton density changes from $\nu_X\approx0.3$ to 0.45. It suggests a weak antiferromagnetic exchange interaction between the distant local moments in the monolayer. The result highlights the strong interlayer correlation effect in this system.

In conclusion, we have realized equilibrium exciton fluids in a lattice using the platform of semiconductor moiré heterostructures. Future studies involving Coulomb drag and counterflow measurements are required to establish the bosonic ground states, investigate the BEC-BCS crossover, and understand the effects of mismatched electron and hole masses. Intermediate hBN spacer thickness (2 nm), which suppresses single-particle interlayer tunneling while maintaining strong interlayer Coulomb correlation, is a promising parameter region to explore. Our results pave the path for the realization of exotic correlated bosonic states, such as excitonic Mott insulator [16, 17], Wigner solid [18, 21], supersolid [18-21] and FFLO state under finite electron-hole density imbalance [54].

Acknowledgements

This study was supported by the US Office of Naval Research under award number N00014-21-1-2471 (capacitance measurement), the Air Force Office of Scientific Research under award number FA9550-18-1-0480 (device fabrication), the National Science Foundation (NSF) under DMR-2004451 (data analysis), and the US Department of Energy (DOE), Office of Science, Basic Energy Sciences (BES) under award no. DE-SC0022058 (optical measurement) and DE-SC0019481 (bulk crystal growth). Growth of the hBN crystals was supported by the Elemental Strategy Initiative of MEXT, Japan and CREST (JPMJCR15F3), JST. This work made use of the Cornell NanoScale Facility, an NNCI member supported by NSF Grant NNCI-1542081.

Author contributions

J.G. fabricated the devices, performed the optical measurements and analysed the data. J.G. and L.M. performed the capacitance measurements and analysed the compressibility data. S.L. and J.C.H. grew the bulk WSe_2 crystals. K.W. and T.T. grew the bulk hBN crystals. J.G., J.S. and K.F.M. designed the scientific objectives and oversaw the project. All authors discussed the results and commented on the manuscript.

Competing interests

The authors declare no competing interests.

Figures

Figure 1 | Semiconductor heterostructures for realization of a dipolar exciton fluid in a lattice. a. Schematic of a dual-gated heterostructure consisting of a WSe_2 monolayer and a WSe_2/WS_2 moiré layer that are separated by 2-4 layers of hBN. The top and bottom gate voltages (V_t and V_b) control the doping density, ν, and the out-of-plane electric field, E, in the heterostructure. **b.** Schematic valence band alignment in the absence of electric field. The dashed line denotes the Fermi level. **c.** Reflection contrast spectrum at ν = 0 and E = -34 mV/nm from device 1, showing two moiré excitons and the 1s and 2s excitons of the monolayer. **d.** Left: electronic Mott insulator at ν = 1 (one hole per moiré site) when all the holes reside in the moiré layer in the absence of electric field; Middle: some of the holes are transferred to the WSe_2 monolayer under a positive electric field. They are tightly bound to the empty moiré sites to minimize the total Coulomb repulsion energy. Right: the empty sites in the moiré layer are equivalent to electrons under a particle-hole transformation. A dipolar exciton fluid in the moiré lattice emerges. **e, f.** Reflection contrast (**e**) and PL (**f**) spectrum of the heterostructure as a function of doping density at E = - 34 mV/nm.

Figure 2 | Optical responses under an out-of-plane electric field. Optical reflection spectrum of the 1s exciton of the monolayer (**a**) and the PL spectrum of the moiré layer (**b**) versus doping density (device 1). The out-of-plane electric field is -10, 15, 18, and 30 mV/nm, respectively, from the top to the bottom row. Upon doping in the monolayer, the 1s exciton feature turns into an attractive polaron (redshifted branch, X^+) and a repulsive polaron (blueshifted branch, not labeled). The PL of the moiré layer exhibits abrupt energy shift and intensity suppression at the correlated insulating states. A new correlated insulating state is observed at ν = 1 under E = 15 and 18 mV/nm; it can no longer be identified at E = 30 mV/nm.

Figure 3 | Excitonic insulator at $\boldsymbol{\nu = 1}$. Peak PL intensity of the moiré layer (**a**) and peak reflection amplitude of the monolayer 1s exciton (**b**) as a function of doping density and electric field from device 1. The four regions (I-IV) are defined by the electrostatic doping density in the monolayer (ν_f) and the moiré layer (ν_m). Region I: ν_f = 0, 0 < ν_m < 1; Region II: $\nu_f > 0$, $\nu_m = 1$; Region III: $\nu_f > 0$, 0 < ν_m < 1; Region IV: $\nu_f > 0$, $\nu_m =$ 0. The boundaries determined by the data in **a** and **b** are shown in dashed and dashdotted lines, respectively. The boundary between region I and II can be determined by either **a** or **b**. A new correlated insulating state is observed at ν = 1 in region III. **c.** Differential bottom-gate capacitance C, in units of the geometrical capacitance C_g, as a function of (ν, E) at 20 K from device 2. Only region III and IV are accessible because of the device structure. A charge-incompressible state is observed at total filling ν = 1. **d.** Charge gap extracted from capacitance as a function of electric field (bottom axis) and doping density (or exciton density, top axis) in the monolayer at varying temperatures. The typical error bars are the propagated uncertainty in the gate-dependent capacitance (vertical) and in the optical determination of the boundary (horizontal).

Figure 4 | Emergence of local magnetic moments in monolayer WSe_2. a. Out-of-plane magnetic-field dependence of MCD at ν = 1 and $\nu_f = \nu_X \approx 0.3$ (at which the heterostructure is an excitonic insulator) for varying temperatures. The spectral dependence of the MCD is determined as the difference between the left- and right-handed reflected light intensity divided by the total reflected light intensity. It is integrated over a narrow spectral range near the repulsive polaron resonance (1.73 eV) as detailed in Methods. **b.** Temperature dependence of the inverse MCD slope around zero magnetic field (which is proportional to the inverse magnetic susceptibility) as a function of temperature at $\nu_f \approx 0.3$ and 0.45. The error bars are estimated from the linear fit to the low-field data in **a**. The magnetic susceptibility follows the Curie-Weiss dependence (solid lines) at high temperatures with small negative Weiss constants (the x-intercepts). The magnitude of the Weiss constant is compatible with weak antiferromagnetic exchange interactions between the distant local moments.

References

1. Andrei, E.Y. et al. The marvels of moiré materials. *Nature Reviews Materials* **6**, 201-206 (2021).
2. Andrei, E.Y. & MacDonald, A.H. Graphene bilayers with a twist. *Nature Materials* **19**, 1265-1275 (2020).
3. Balents, L., Dean, C.R., Efetov, D.K. & Young, A.F. Superconductivity and strong correlations in moiré flat bands. *Nature Physics* **16**, 725-733 (2020).
4. Kennes, D.M. et al. Moiré heterostructures as a condensed-matter quantum simulator. *Nature Physics* **17**, 155-163 (2021).
5. Cao, Y. et al. Unconventional superconductivity in magic-angle graphene superlattices. *Nature* **556**, 43-50 (2018).
6. Chen, G. et al. Tunable correlated Chern insulator and ferromagnetism in a moiré superlattice. *Nature* **579**, 56-61 (2020).
7. Serlin, M. et al. Intrinsic quantized anomalous Hall effect in a moiré heterostructure. *Science* **367**, 900 (2020).
8. Sharpe, A.L. et al. Emergent ferromagnetism near three-quarters filling in twisted bilayer graphene. *Science* **365**, 605 (2019).
9. Huang, X. et al. Correlated insulating states at fractional fillings of the WS2/WSe2 moiré lattice. *Nature Physics* (2021).
10. Regan, E.C. et al. Mott and generalized Wigner crystal states in WSe2/WS2 moiré superlattices. *Nature* **579**, 359-363 (2020).
11. Tang, Y. et al. Simulation of Hubbard model physics in WSe2/WS2 moiré superlattices. *Nature* **579**, 353-358 (2020).
12. Xu, Y. et al. Correlated insulating states at fractional fillings of moiré superlattices. *Nature* **587**, 214-218 (2020).
13. Shimazaki, Y. et al. Strongly correlated electrons and hybrid excitons in a moiré heterostructure. *Nature* **580**, 472-477 (2020).
14. Halperin, B.I. & Rice, T.M. Possible Anomalies at a Semimetal-Semiconductor Transistion. *Reviews of Modern Physics* **40**, 755-766 (1968).
15. Kohn, W. & Sherrington, D. Two Kinds of Bosons and Bose Condensates. *Reviews of Modern Physics* **42**, 1-11 (1970).
16. Bloch, I., Dalibard, J. & Nascimbène, S. Quantum simulations with ultracold quantum gases. *Nature Physics* **8**, 267-276 (2012).
17. Dutta, O. et al. Non-standard Hubbard models in optical lattices: a review. *Reports on Progress in Physics* **78**, 066001 (2015).
18. Joglekar, Y.N., Balatsky, A.V. & Das Sarma, S. Wigner supersolid of excitons in electron-hole bilayers. *Physical Review B* **74**, 233302 (2006).
19. Léonard, J., Morales, A., Zupancic, P., Esslinger, T. & Donner, T. Supersolid formation in a quantum gas breaking a continuous translational symmetry. *Nature* **543**, 87-90 (2017).
20. Li, J.-R. et al. A stripe phase with supersolid properties in spin–orbit-coupled Bose–Einstein condensates. *Nature* **543**, 91-94 (2017).
21. Ya-Hui Zhang, D. N. Sheng & Vishwanath, A. SU(4) chiral spin liquid, exciton supersolid and electric detection in moiré bilayers. *arXiv:2103.09825* (2021).
22. Ma, L. et al. Strongly correlated excitonic insulator in atomic double layers. *arXiv preprint arXiv:2104.05066* (2021).

23. Wang, Z. et al. Evidence of high-temperature exciton condensation in two-dimensional atomic double layers. *Nature* **574**, 76-80 (2019).
24. Pan, H., Wu, F. & Das Sarma, S. Quantum phase diagram of a Moire-Hubbard model. *Physical Review B* **102**, 201104 (2020).
25. Wu, F., Lovorn, T., Tutuc, E. & MacDonald, A.H. Hubbard Model Physics in Transition Metal Dichalcogenide Moire Bands. *Physical Review Letters* **121**, 026402 (2018).
26. Burg, G.W. et al. Strongly Enhanced Tunneling at Total Charge Neutrality in Double-Bilayer Graphene-WSe2 Heterostructures. *Physical Review Letters* **120**, 177702 (2018).
27. Eisenstein, J.P. & MacDonald, A.H. Bose–Einstein condensation of excitons in bilayer electron systems. *Nature* **432**, 691-694 (2004).
28. Li, J.I.A., Taniguchi, T., Watanabe, K., Hone, J. & Dean, C.R. Excitonic superfluid phase in double bilayer graphene. *Nature Physics* **13**, 751-755 (2017).
29. Liu, X., Watanabe, K., Taniguchi, T., Halperin, B.I. & Kim, P. Quantum Hall drag of exciton condensate in graphene. *Nature Physics* **13**, 746-750 (2017).
30. Nandi, D., Finck, A.D.K., Eisenstein, J.P., Pfeiffer, L.N. & West, K.W. Exciton condensation and perfect Coulomb drag. *Nature* **488**, 481-484 (2012).
31. Butov, L.V. Condensation and pattern formation in cold exciton gases in coupled quantum wells. *Journal of Physics: Condensed Matter* **16**, R1577-R1613 (2004).
32. Snoke, D. Spontaneous Bose Coherence of Excitons and Polaritons. *Science* **298**, 1368 (2002).
33. Yu. E. Lozovik & Yudson, V.I. A new mechanism for superconductivity: pairing between spatially separated electrons and holes. *Zh. Eksp. Teor. Fiz.* **71**, 738-753 (1976).
34. Perali, A., Neilson, D. & Hamilton, A.R. High-Temperature Superfluidity in Double-Bilayer Graphene. *Physical Review Letters* **110**, 146803 (2013).
35. Conti, S., Van der Donck, M., Perali, A., Peeters, F.M. & Neilson, D. Doping-dependent switch from one- to two-component superfluidity in coupled electron-hole van der Waals heterostructures. *Physical Review B* **101**, 220504 (2020).
36. Fogler, M.M., Butov, L.V. & Novoselov, K.S. High-temperature superfluidity with indirect excitons in van der Waals heterostructures. *Nature Communications* **5**, 4555 (2014).
37. Wu, F.-C., Xue, F. & MacDonald, A.H. Theory of two-dimensional spatially indirect equilibrium exciton condensates. *Physical Review B* **92**, 165121 (2015).
38. Conti, S., Neilson, D., Peeters, F.M. & Perali, A. Transition Metal Dichalcogenides as Strategy for High Temperature Electron-Hole Superfluidity. *Condensed Matter* **5**, 22 (2020).
39. Xiaomeng Liu et al. Crossover between Strongly-coupled and Weakly-coupled Exciton Superfluids. *arXiv:2012.05916* (2020).
40. Alexeev, E.M. et al. Resonantly hybridized excitons in moiré superlattices in van der Waals heterostructures. *Nature* **567**, 81-86 (2019).
41. Jin, C. et al. Observation of moiré excitons in WSe2/WS2 heterostructure superlattices. *Nature* **567**, 76-80 (2019).
42. Seyler, K.L. et al. Signatures of moiré-trapped valley excitons in MoSe2/WSe2 heterobilayers. *Nature* **567**, 66-70 (2019).

43. Tran, K. et al. Evidence for moiré excitons in van der Waals heterostructures. *Nature* **567**, 71-75 (2019).
44. Wu, F., Lovorn, T. & MacDonald, A.H. Topological Exciton Bands in Moir\'e Heterojunctions. *Physical Review Letters* **118**, 147401 (2017).
45. Ruiz-Tijerina, D.A. & Fal'ko, V.I. Interlayer hybridization and moir\'e superlattice minibands for electrons and excitons in heterobilayers of transition-metal dichalcogenides. *Physical Review B* **99**, 125424 (2019).
46. McDonnell, L.P. et al. Superposition of intra- and inter-layer excitons in twistronic MoSe2/WSe2 bilayers probed by resonant Raman scattering. *2D Materials* **8**, 035009 (2021).
47. Jin, C. et al. Stripe phases in WSe 2/WS 2 moiré superlattices. *Nature Materials*, 1-5 (2021).
48. Sidler, M. et al. Fermi polaron-polaritons in charge-tunable atomically thin semiconductors. *Nature Physics* **13**, 255-261 (2017).
49. Efimkin, D.K. & MacDonald, A.H. Many-body theory of trion absorption features in two-dimensional semiconductors. *Physical Review B* **95**, 035417 (2017).
50. Li, T. et al. Charge-order-enhanced capacitance in semiconductor moir\'e superlattices. *arXiv preprint arXiv:2102.10823* (2021).
51. Li, T. et al. Continuous Mott transition in semiconductor moir\'e superlattices. *arXiv preprint arXiv:2103.09779* (2021).
52. Mak, K.F., Xiao, D. & Shan, J. Light–valley interactions in 2D semiconductors. *Nature Photonics* **12**, 451-460 (2018).
53. Stier, A.V., McCreary, K.M., Jonker, B.T., Kono, J. & Crooker, S.A. Exciton diamagnetic shifts and valley Zeeman effects in monolayer WS2 and MoS2 to 65 Tesla. *Nature Communications* **7**, 10643 (2016).
54. Pieri, P., Neilson, D. & Strinati, G.C. Effects of density imbalance on the BCS-BEC crossover in semiconductor electron-hole bilayers. *Physical Review B* **75**, 113301 (2007).

Methods

Device fabrications

We fabricate dual-gate devices of transition metal dichalcogenide (TMD) heterostructures using the reported layer-by-layer dry transfer technique [55]. Details have been reported in earlier studies [11, 12, 56]. The capacitance devices are fabricated following the design in Ref. [50]. Figure 1a shows the cross-section schematic of the devices. Extended Data Fig. 1 shows an optical image of device 1, the optical studies of which are presented in the main text. In particular, the WSe_2 monolayers are exfoliated from bulk crystals grown by the flux growth method [57]; and the WS_2 monolayers are from bulk crystals grown by the chemical vapor transport method (from HQ Graphene). Angle alignment of the WSe_2 and WS_2 monolayers in the moiré bilayer is achieved with assistance of the second harmonic generation [11]. Both 0- and 60-degree-aligned WSe_2/WS_2 bilayers are involved in this study; no noticeable difference is observed in the two cases. The Coulomb-coupled WSe_2 monolayer is not angle aligned. The thickness of the hBN spacer between the moiré layer and the WSe_2 monolayer varies between 2 and 4 layers in different devices. No obvious dependence on the spacer thickness is observed, which is consistent with significant suppression of interlayer tunneling as well as negligible moiré printing on the monolayer. The top and bottom gates are nearly symmetric; they consist of hBN gate dielectrics and few-layer graphite gate electrodes; the thickness of the gate dielectrics is typically between 10 and 40 nm. Few-layer graphite is also used as contact electrodes in devices used for the optical studies. Pt electrodes are used to achieve better p-type contacts to the TMD heterostructures for the AC capacitance studies.

Optical measurements

The devices are characterized by the optical reflection, magnetic circular dichroism (MCD) and photoluminescence (PL) spectroscopies. They are mounted in an AttoDry 1000 cryostat. In the optical reflection measurements [11, 12], we focus white light from a tungsten halogen lamp onto the devices with a micron spot size using an optical microscope objective with numerical aperture 0.8. The incident power is less than 1 nW. The reflected light from the devices is collected by the same objective and sent to a spectrometer equipped with a charge-coupled device (CCD) for spectrum analysis. To obtain the reflection contrast spectrum, we use as a reference the reflected light intensity from the sample at a large hole or electron doping density, for which all the exciton features become negligible. We use the same setup for the MCD measurements in the polar geometry; the magnetic field is out-of-plane; the incident white light is circularly polarized (details see [11, 51]). The MCD spectrum is defined as the difference between the left- and right-handed reflected light intensity divided by the total reflected light intensity. Extended Data Fig. 3 shows the MCD spectrum as a function of magnetic field at several representative electric fields and fixed total doping density $\nu = 1$. We focus on the spectral range of the attractive and repulsive polarons of the monolayer. MCD is not observed at zero magnetic field; it increases monotonically with magnetic field and saturates around 2-3 T. The MCD is resonantly enhanced near the energy of both the repulsive and attractive polarons; it changes sign across the polaron resonances, which is consistent with the reported results [11, 51]. We integrate the MCD signal over a narrow spectral window (boxed) near the repulsive polaron resonance to obtain Fig. 4 in the main text. The integrated MCD is proportional the valley magnetization of the carriers in the WSe_2 monolayer [11, 51]. For the PL measurements, we employ a He-Ne laser (633 nm) as the excitation source; the incident power is 30 nW.

Capacitance measurements

We follow the design reported in Ref. [50] to achieve good electrical contacts to the TMD heterostructure for the capacitance measurements. Extended Data Fig. 4a shows the schematic. The top gate (the global gate) covers the entire TMD heterostructure; the bottom gate (the local gate) covers it partially. The overlapped area is the region of interest; the non-overlapped area is the contact region. A negative voltage is applied to the global gate to introduce holes into the entire TMD heterostructure; the bottom local gate depletes holes in the region of interest (red box). The device structure limits the range of (ν, E) that can be accessed in the capacitance study because a finite negative top gate voltage is required to maintain hole doping in the contact region to achieve good electrical contacts.

The TMD heterostructure is DC-grounded. An AC excitation voltage (amplitude = 10 mV and frequency = 443-3317 Hz) is applied to the TMD heterostructure. Charge is collected from the bottom gate and sent to an on-chip high-electron-mobility transistor (HEMT) amplifier and lockin for detection [58]. The differential capacitance C is the ratio of the collected charge to the excitation voltage. We verify that the result is largely independent of the excitation frequency.

Extended Data Fig. 4b shows C in the units of C_g as a function of (ν, E) at 20 K, where C_g is the geometrical capacitance defined by the thickness and dielectric constant of the hBN layer between the bottom gate and the TMD heterostructure. The electrostatic doping regions are determined by optical responses in Extended Data Fig. 4c, d. Only region III and IV can be accessed. The diagonal dashed green line corresponds to constant top-gate voltage -1.4 V. It marks the onset of charging into the device. Top-gate voltage above the green line is required to dope the contact region and turn on the channel for capacitance measurements.

Extended Data Fig. 4c shows the PL peak intensity from the moiré layer as a function of (ν, E). The PL intensity is sensitive to doping in the moiré layer [11, 47]. The dashed line marks the boundary between Region III and IV, corresponding to doped and neutral moiré layer, respectively. Extended Data Fig. 4d shows the peak reflection contrast of the monolayer 1s exciton, which is sensitive to doping in the monolayer [23, 48]. The black dashed line marks the onset of hole doping in the monolayer. It is consistent with the onset of finite capacitance signal (Extended Data Fig. 4b). A change in the 1s reflection contrast is also observed across the green dashed line, which marks the onset of charging into the device. Detailed discussions on the electrostatic doping regions are provided below.

The measured differential capacitance accesses the quantum capacitance, C_Q, of the TMD heterostructure, which represents its electronic compressibility, by $\frac{1}{C} \approx \frac{2}{C_Q} + \frac{1}{C_g}$ [50]. We expect $C \approx C_g$ for a charge-compressible state and $C < C_g$ for a charge-incompressible state. A charge-incompressible state is clearly observed at $\nu = 1$ over an extended range of electric field. The state weakens with increasing electric field. This is fully consistent with the optical results (Extended Data Fig. 7). The absence of a charge-incompressible state at the moiré filling $\nu_m = 1$ also shows negligible moiré printing onto the monolayer from the moiré layer.

We perform temperature dependence studies of the capacitance. Extended Data Fig. 5 shows the results at 20, 40, 60, 80, 120, and 150 K. With increasing temperature, the charge-incompressible state at $\nu = 1$ becomes weaker and vanishes around 120 K. This corresponds to thermal ionization of the excitons; the exciton fluid turns into electron-hole plasma, which are charge-compressible [22]. The charge-incompressible state at smaller electric field (corresponding to smaller exciton density) persists to higher temperatures, that is, the exciton ionization temperature or binding energy increases with decreasing density. This is consistent with the exciton Mott transition, at which the exciton binding energy drops to zero [22, 36, 59].

Electrostatics phase diagram

Extended Data Fig. 6 shows the electrostatics phase diagram with a larger parameter range for (ν, E) than Fig. 3 in the main text. Extended Data Fig. 6a-c are the (peak) PL intensity of the moiré layer, the (peak) reflection intensity of the 1s exciton and the attractive polaron of the WSe_2 monolayer, respectively. The dashed lines outline the boundaries of different electrostatic doping regions. Below we describe how these boundaries are determined from the spectral responses.

We first examine the 1s exciton reflection (Extended Data Fig. 6b). The feature is sensitive to doping in the monolayer [23, 48]. We can draw the boundary between the charge-neutral (red) and hole-doped region (blue) based on the 1s response. The boundary is also schematically shown in Extended Data Fig. 6d as the blue line. Along the line the monolayer remains charge neutral ($\nu_f = 0$) and holes are doped solely into the moiré layer ($\nu = \nu_m$). The line traces the valence band edge of the monolayer as it shifts across the Hubbard bands of the moiré layer under an applied electric field. It therefore probes the chemical potential as a function of doping density of the moiré layer. In particular, the boundary is vertical over a range of electric field, ΔE, when the monolayer band edge is located inside a charge gap of the moiré layer. The product of ΔE and the separation between the monolayer and the moiré layer, d, corresponds approximately to the charge gap energy. When the monolayer band edge overlaps with a Hubbard band, the boundary line gains a finite slope, which is inversely proportional to the thermodynamic density of states of the particular Hubbard band. Our data shows that the $\nu_m = 1$ Mott gap is about twice the $\nu_m = 2$ moiré band gap, and the first Hubbard band is flatter than the second. These results are fully consistent with the reported properties of angle-aligned WSe_2/WS_2 bilayers [12].

The map of the attractive polaron response is expected to be complementary to that of the 1s exciton since a charge-neutral monolayer gives rise to strong 1s exciton and weak attractive polaron reflection [23, 48]; these spectral responses are reversed for a doped monolayer. This is consistent with our experimental results of Extended Data Fig. 6b,c.

Next we examine the PL intensity from recombination of holes in WSe_2 and electrons in WS_2 of the moiré layer (Extended Data Fig. 6a). Large PL intensity (red) is observed when the moiré layer is charge neutral ($\nu_m = 0$). A local PL intensity minimum emerges when the Fermi level touches a Hubbard band. The results are consistent with recent studies [11, 47]. We draw the boundaries of the Hubbard bands (both their top and bottom) by following the PL local minimum. The boundaries of the first and second Hubbard bands are also shown schematically as orange lines in Extended Data Fig. 6d. The solid and dashed lines denote the top and bottom of a Hubbard band, respectively. Similar to the analysis of the 1s exciton above, the boundaries correspond to constant filling of the moiré layer at ν_m= 0, 1, or 2 and doping into the monolayer with $\nu_f = \nu - \nu_m$. Each orange line traces a Hubbard band edge as it moves relative to the monolayer valence band. It probes the thermodynamic equation of state of the monolayer. Because there is only one semiconductor charge gap around 2 eV in the monolayer, each Hubbard band edge gives only one vertical line when it moves inside the monolayer gap. Outside the monolayer band gap, the finite slope of the orange line is inversely proportional to the thermodynamic density of states of the monolayer.

We summarize the distinct regions of the electrostatics phase diagram shown in Extended Data Fig. 6.

- Region I: $\nu_f = 0$ and $\nu = \nu_m$. No electric field dependence is seen here because all of the holes reside in the moiré layer. Electron crystal states can be clearly identified as vertical straight lines at fractional filling factors. The PL features below $\nu \approx 1/3$ are likely artifacts from the nonlinear charging effect.
- Region II: $\nu_m = 1$ and $\nu_f = \nu - 1$. Here the Fermi level is inside the Mott gap of the moiré layer.
- Region III (region of interest): $\nu_f > 0$ and $\nu_m < 1$. Both layers are hole-doped and the applied electric field transfers holes between the layers. The electron crystal states disappear in this region because of hole screening from the WSe_2 monolayer.
- Region IV: $\nu_m = 0$ and $\nu = \nu_f$.

Similarly, we can assign regions I', II' and III', which are the second Hubbard band copies of regions I, II and III. They correspond to ($\nu_f = 0$ and $\nu = \nu_m$), ($\nu_m = 2$ and $\nu_f = \nu - 2$) and ($\nu_f > 0$, $1 < \nu_m < 2$), respectively.

Data availability
Source data are provided with this paper. The data that support the findings of this study are available from the corresponding authors upon reasonable request.

Code availability
The code that supports the plots in this paper is available from the corresponding author upon reasonable request.

References
55. Wang, L. et al. One-Dimensional Electrical Contact to a Two-Dimensional Material. *Science* **342**, 614 (2013).
56. Xu, Y. et al. Creation of moiré bands in a monolayer semiconductor by spatially periodic dielectric screening. *Nature Materials* **20**, 645-649 (2021).
57. Gustafsson, M.V. et al. Ambipolar Landau levels and strong band-selective carrier interactions in monolayer WSe2. *Nature Materials* **17**, 411-415 (2018).
58. Ashoori, R.C. et al. Single-electron capacitance spectroscopy of discrete quantum levels. *Physical Review Letters* **68**, 3088-3091 (1992).
59. López Ríos, P., Perali, A., Needs, R.J. & Neilson, D. Evidence from Quantum Monte Carlo Simulations of Large-Gap Superfluidity and BCS-BEC Crossover in Double Electron-Hole Layers. *Physical Review Letters* **120**, 177701 (2018).

Fig. 1

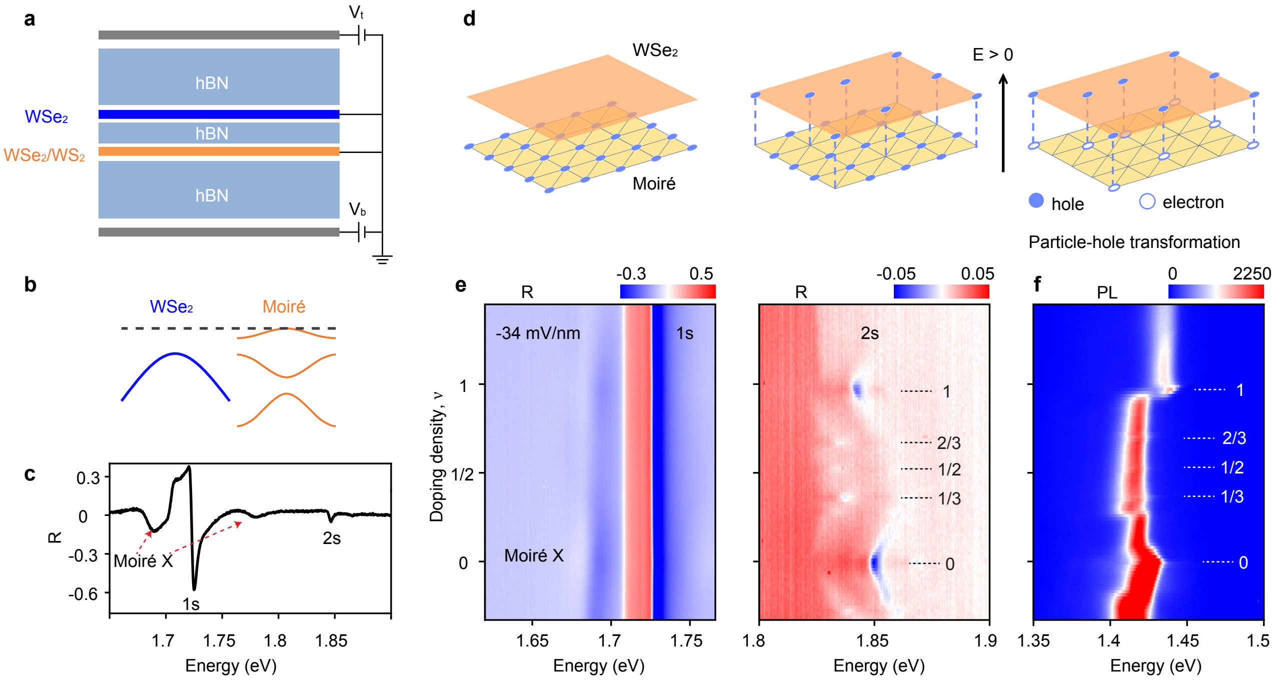
a
Vt
hBN
WSe2
hBN
WSe2/WS2
hBN
Vb
b
WSe2
Moiré
c
0.3
0
-0.3
-0.6
R
Moiré X
1s
2s
1.7
1.75
1.8
1.85
Energy (eV)
d
WSe2
Moiré
E > 0
hole
electron
Particle-hole transformation
e
R
-0.3
0.5
-34 mV/nm
1s
Moiré X
Doping density, ν
1
1/2
0
1.65
1.7
1.75
Energy (eV)
R
-0.05
0.05
2s
1
2/3
1/2
1/3
0
1.8
1.85
1.9
Energy (eV)
f
PL
0
2250
1
2/3
1/2
1/3
0
1.35
1.4
1.45
1.5
Energy (eV)

Fig. 2

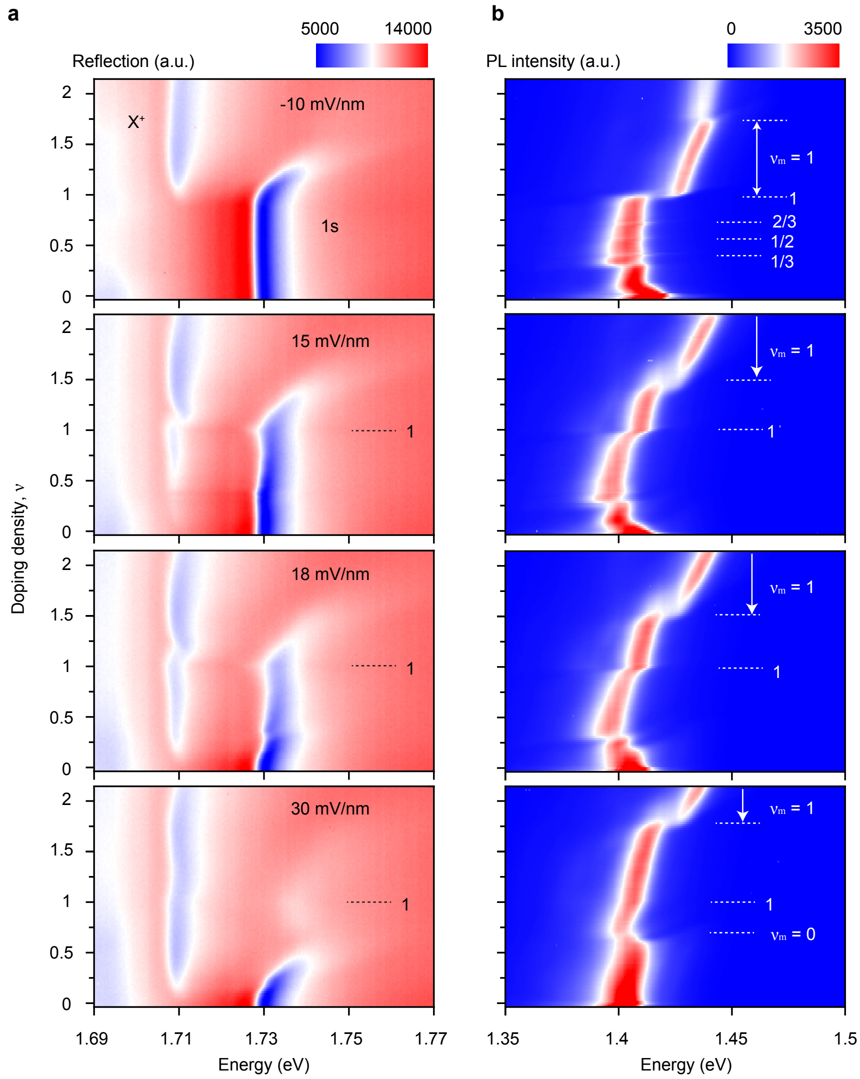
a
Reflection (a.u.)
5000
14000
X+
-10 mV/nm
1s
15 mV/nm
18 mV/nm
30 mV/nm
1
Doping density, ν
Energy (eV)
b
PL intensity (a.u.)
0
3500
νm = 1
1
2/3
1/2
1/3
νm = 0
Energy (eV)

Fig. 3

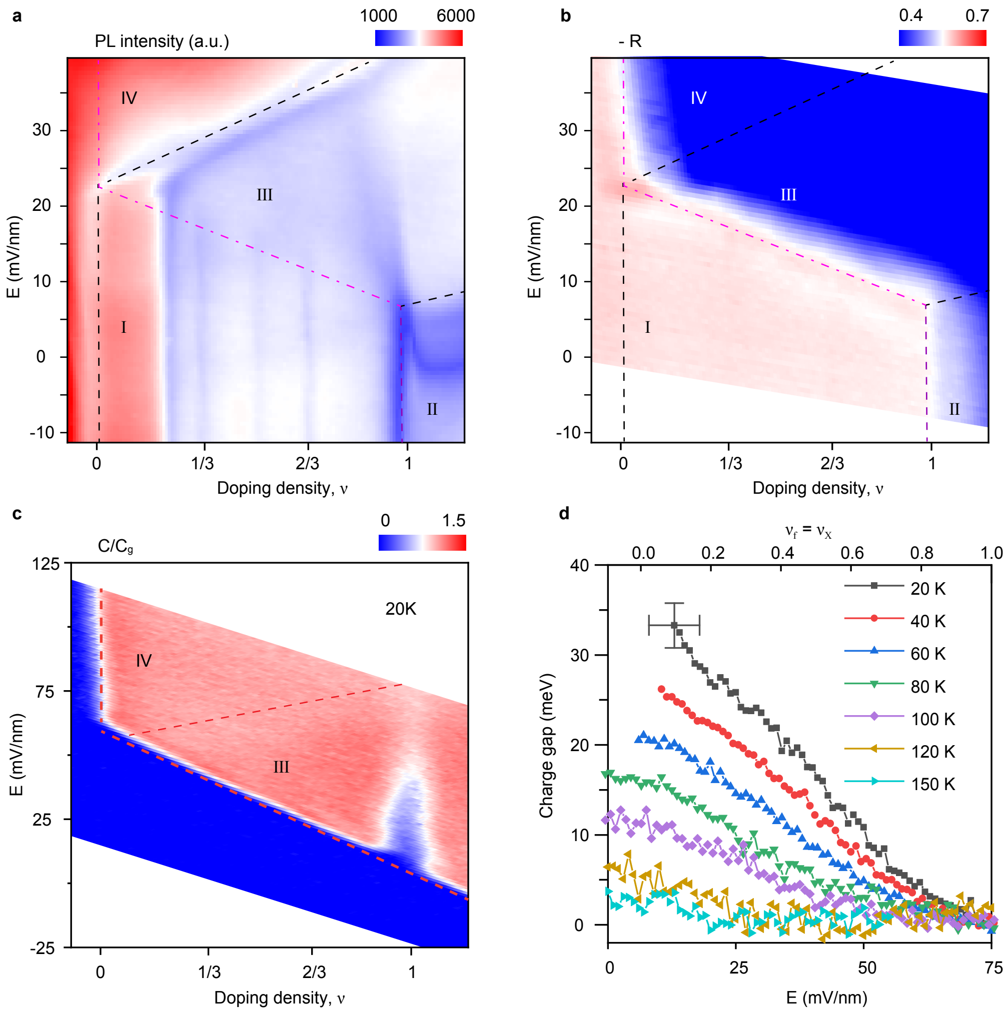

a
PL intensity (a.u.)
1000
6000
IV
III
I
II
E (mV/nm)
Doping density, ν
b
- R
0.4
0.7
IV
III
I
II
E (mV/nm)
Doping density, ν
c
C/C$_g$
0
1.5
20K
IV
III
E (mV/nm)
Doping density, ν
d
ν$_f$ = ν$_X$
20 K
40 K
60 K
80 K
100 K
120 K
150 K
Charge gap (meV)
E (mV/nm)

Fig. 4

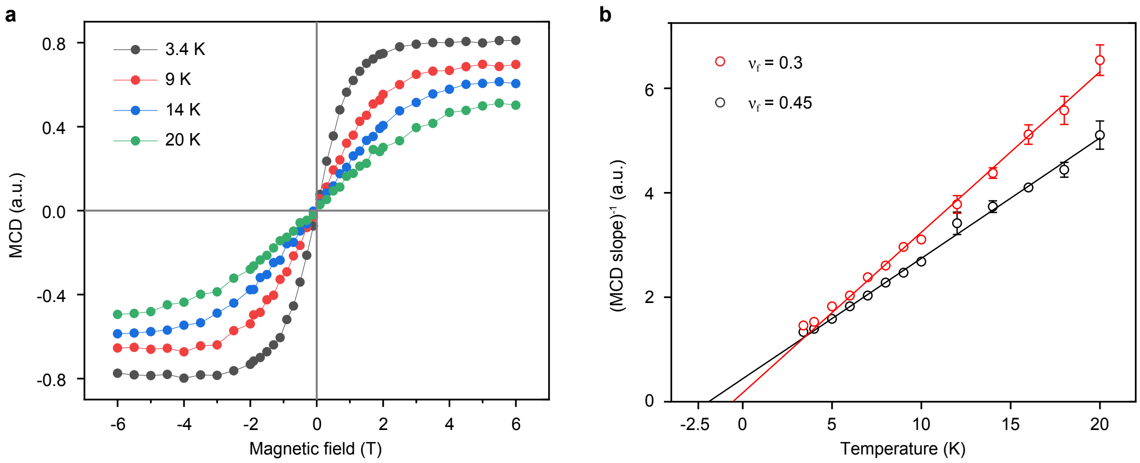
a
3.4 K
9 K
14 K
20 K
MCD (a.u.)
0.8
0.4
0.0
-0.4
-0.8
-6
-4
-2
0
2
4
6
Magnetic field (T)
b
ν_f = 0.3
ν_f = 0.45
(MCD slope)$^{-1}$ (a.u.)
6
4
2
0
-2.5
0
5
10
15
20
Temperature (K)

Ex, Data Fig. 1

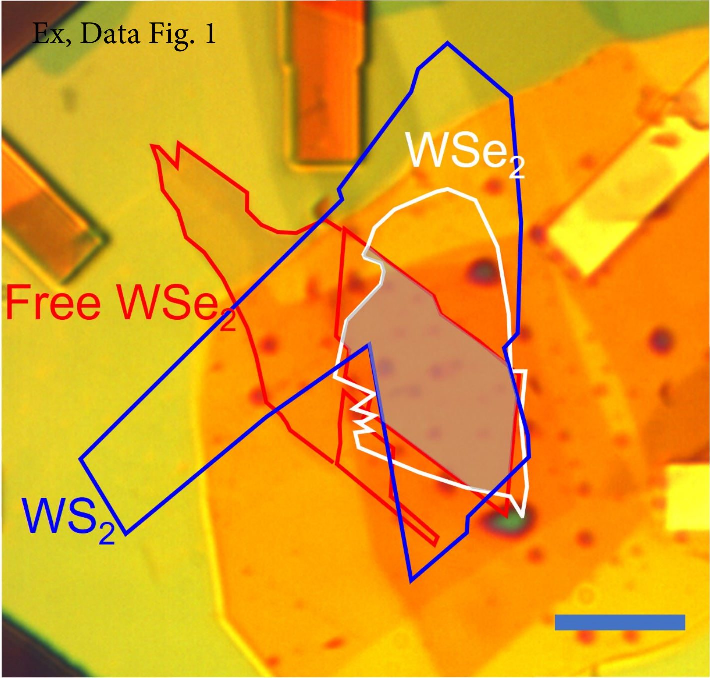

Ext. Data Fig. 2

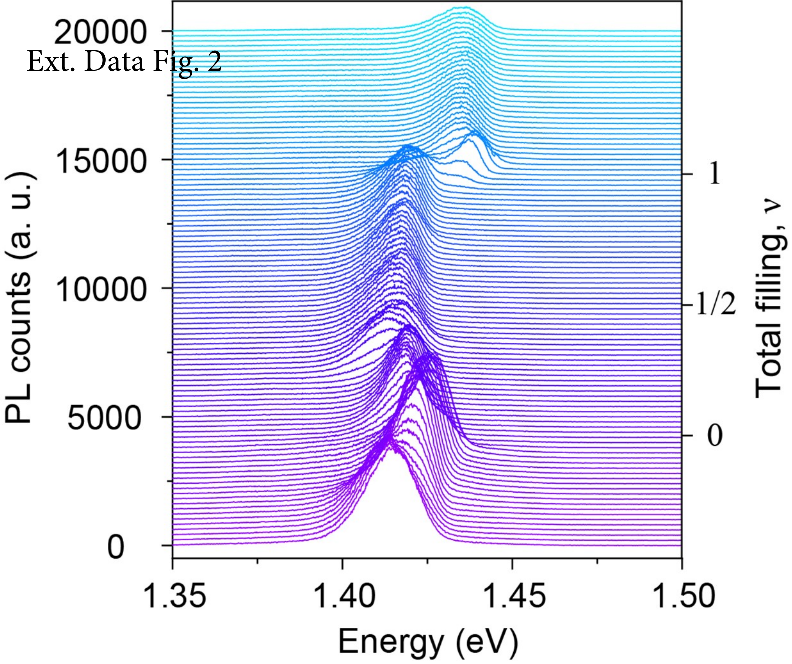

Ext. Data Fig. 3

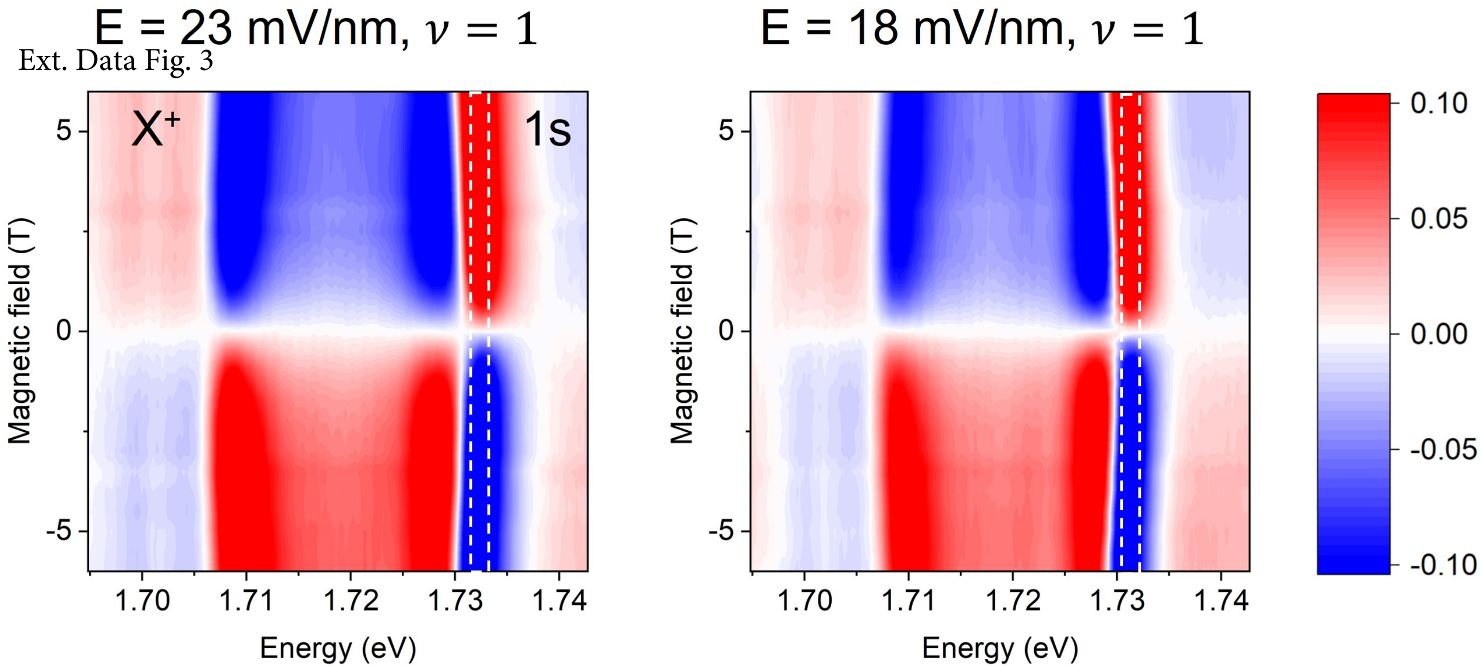

Ext. Data Fig. 4

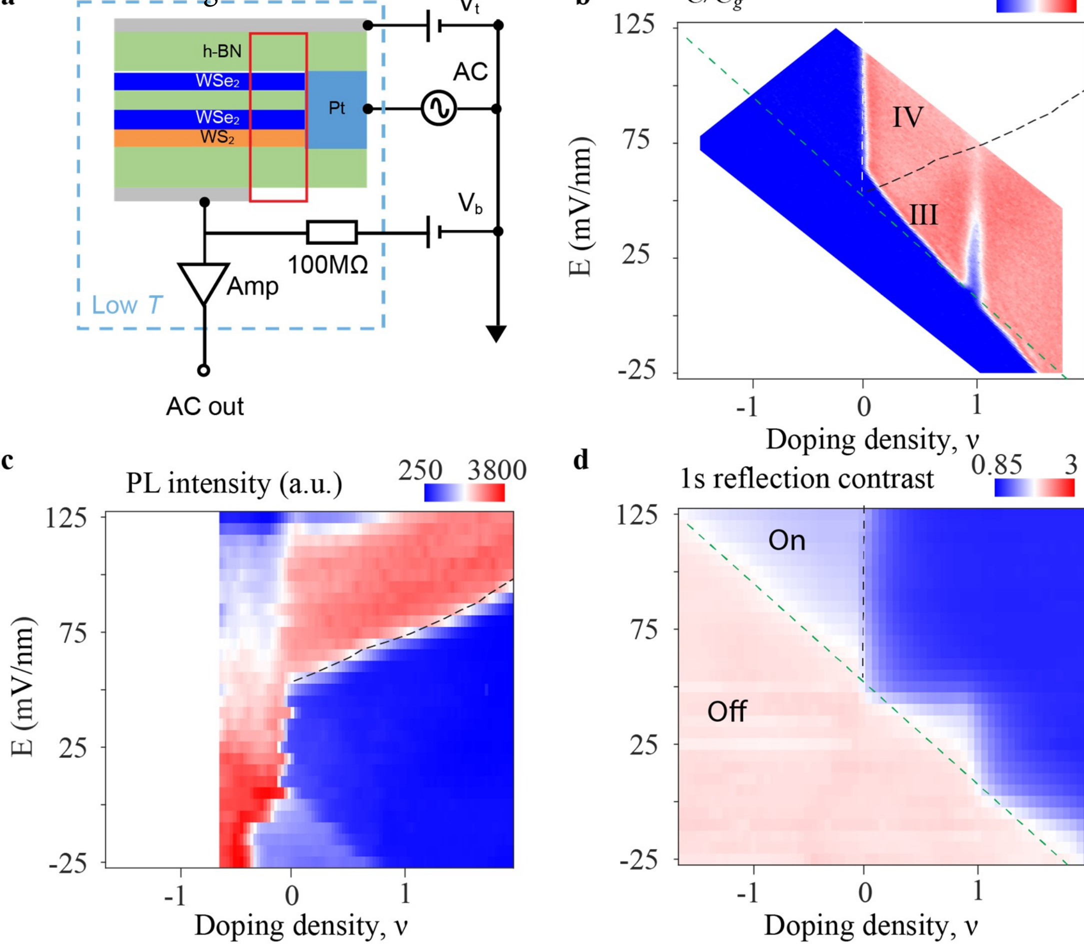

Ext. Data Fig. 5

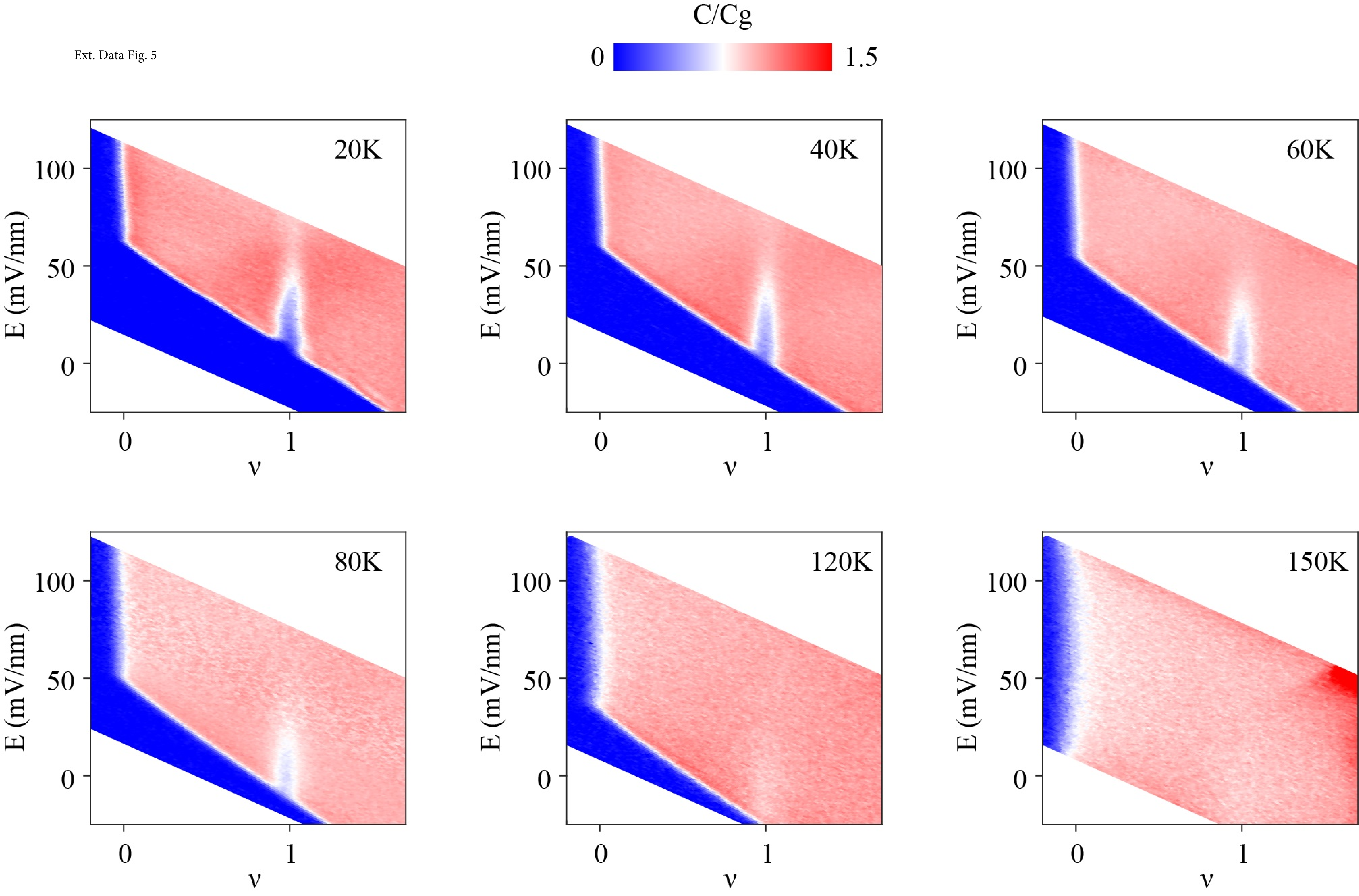

Ext. Data Fig. 6

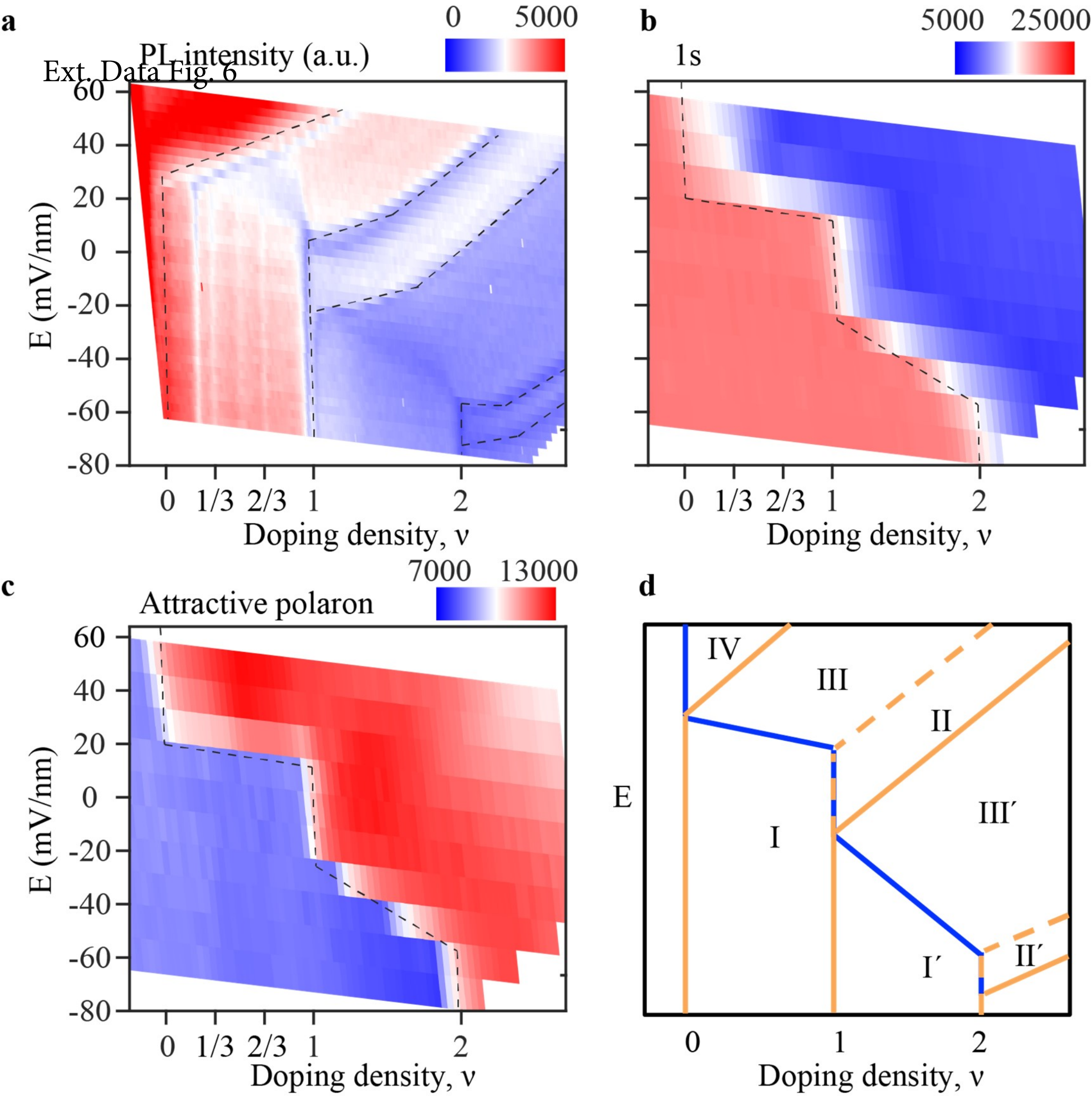

Ext. Data Fig. 7